Journal of Applied Fluid Mechanics, Vol. 17, No. 9, pp. 1844-1859, 2024.
Available online at www.jafmonline.net, ISSN 1735-3572, EISSN 1735-3645.
https://doi.org/10.47176/jafm.17.9.2473

Experimental and Numerical Investigation for Predicting the Performance of Voluteless Centrifugal Fan Rotors

D. O. Maestre Di Cioccio†, W. de Oliveira and R. G. Ramirez Camacho

Federal University of Itajubá, Itajubá, Minas Gerais, Zip Code 37500-903, Brazil

†Corresponding Author Email: darwin.maestre@unifei.edu.br

ABSTRACT

A better understanding of the flow field is crucial for improving the design of a turbomachine. In this work we investigate the performance of voluteless centrifugal fan rotors. The study includes two parts: experiments and numerical simulations through Computational Fluid Dynamics (CFD) techniques. Our test system allows the analysis of the flow behavior of centrifugal fan rotors maintaining the meridional shape without making substantial changes to their internal structure, but with different blade shapes, sizes, and blade numbers. To avoids irregular interference with the rotor flow from external components such as the collector a radial channel composed by two parallel discs was placed concentrically on the rotor axis at its outer periphery with special interest in measuring flow characteristics at the rotor outlet with a reliable accuracy. As an application case a typical centrifugal fan rotor with ten blades of single curvature in the circular arc shape has been investigated. Two types of measuring systems were used: one, with an aerodynamic probe located in the centrifugal rotor outlet and, the other, with a load cell for measuring the rotor shaft power. A comparison of the results by these two measuring arrangements shows some important characteristics, such as the phenomenon of the flow recirculation within the rotor. The experimental performance curves related to non-dimensional flow such as the slip factor, and pressure coefficient, revealed good matching with numerical simulations, highlighting the remarkable reliability of our experimental setup.

Article History

Received December 2, 2023
Revised March 13, 2024
Accepted March 19, 2024
Available online July 2, 2024

Keywords:

CFD analysis
Centrifugal rotor
Performance test
Experimental techniques
SST k-w turbulence model

1. INTRODUCTION

Centrifugal fans are widely utilized in diverse industrial applications, including heating, ventilation, air conditioning, cooling units, and various other industrial purposes. They excel at generating a relatively high total pressure rise with low flow rates, setting them apart from axial and diagonal flow turbomachines. Applications of fans without a casing or volute surrounding the rotor are known as unhoused, volute-free, or isolated centrifugal fans. This treatment enables the advantage to explore the reduction of flow losses and noise reduction while emphasizing the direct interaction between the rotor and the outlet.

Many authors and engineers have studied the flow characteristics of centrifugal rotors surrounded by a volute. Most of them centered on numerical calculations of aerodynamic sound generating mechanism and tonal noise reduction (Meakhail & Park, 2004; Datong et al., 2009; Zhang et al., 2016; Wei et al., 2019). In the context of voluteless centrifugal fans, recent studies, such as those by Carolus et al. (2000), Cui and Chen (2017), Ottersten et al. (2018), and Ottersten et al. (2021), have primarily focused on the numerical prediction of flow and experimental techniques addressing noise generation mechanisms, tonal noise prediction and the effects of the installation of a driven motor at the impeller eye on the performance, as studied by Cui and Chen (2017). However, it is worth noting that, until now, the experimental techniques employed in these works have consistently involved advanced and costly resources such as hot-wire and laser anemometry, pressure transmitters, imaging techniques, etc. However, the achievement of such modern techniques becomes a difficult task if the balance between resources and practicality is considered.

Beyond noise prediction, flow, and aerodynamic quantities also play a crucial role in studying the performance of these types of rotors. The main novelty of

NOMENCLATURE

a	constant parameters to non-linear parameters estimation	TAL	Blades in a shape where the tangent of the constructive angle of the blades varies linearly with the radius of the rotor
ARC	Circular Arc Shape	r	radius
BEP	Best Efficiency Point	M_a	Mach number
b	blade width	x	radius ratio
c	absolute velocity	u	tangential velocity
c_a	absolute velocity component in the axial direction	w	relative velocity
c_m	meridional component velocity	Y	rotor specific work
c_u	absolute velocity component in the u direction	y^+	dimensionless distance
D	rotor diameter	θ_c	critical angle
e_b	blade thickness	β	blade angle
f_e	geometric choking factor	ε	slip factor
g	gravitational acceleration	ψ	pressure coefficient
h_e	static pressure	α	absolute flow angle
h_s	stagnation pressure	Δ_{pt}	total pressure rise
HVAC	Heating, Ventilation, and Air Conditioning	$\in$	residual mean square (RMS)
HIP	Hyperbolic Blade Format	λ	power coefficient $\lambda = \psi\phi/\eta$; angle
m	number of points	ϕ	flow coefficient
N	number of blades	η	rotor efficiency
n_{qA}	specific rotation according to Addison	ρ	fluid density
n	angular velocity in [rpm] or [rps]	θ_p	probe position angle
LOG	Logarithmic Blade Format	ω	angular velocity; specific energy dissipation rate
RET	straight format	k	turbulent kinetic energy

this work is to provide a reliable test method for studying the aerodynamic characteristics and flow quantities in a simple manner using a single-hole pitot probe. This probe measures flow direction, magnitude, and static pressure values at the rotor outlet in a test section where a key feature is maintaining symmetrical flow within the rotor. This ensures that internal components do not disrupt the flow irregularly, as might occur in testing with a volute.

This approach can lead to a deeper understanding of various local and global quantities, both at the design point and off-design, ultimately helping to improve the performance of these arrangements. The specific test section is designed to test rotors with diverse geometries. The rotors can maintain the same meridional shape and constant width while variations can be made in the quantity, sizes, and shape of their blades. Each blade shapes following the sample of the Fig.1 can be tested, and its attachment on each disk can done using screws to facilitate the interchangeability of both the number and the shape of the blades to all needed configurations.

2. APPLICATION CASE

2.1 Tested Rotor and Experimental Facility

A centrifugal fan rotor, depicted in Fig. 2, was selected as the subject of research for demonstration purposes and was addressed and designed to carry out the experiments. It has a specific rotation according to Addison of $n_{qA} = 150$, being n_{qA} represented by Eq.1.

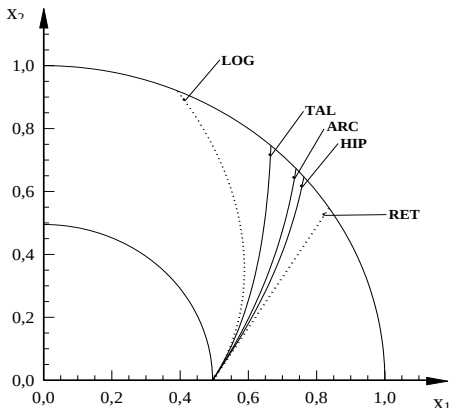

Fig. 1 Schematic blade shape configuration

$$n_{qA} = 10^3 \frac{nQ^{1/2}}{Y^{3/4}} \quad (1)$$

where Q, is the design flow rate, Y, the specific work of the rotor and n is the rotation speed.

The blades are swept backwards with a single curvature in the circular arc shape (ARC) between the inner diameter D_4 and the outer diameter D_5. These blades are attached to the bottom and cover disk. The bottom disc is perpendicular to the axis of rotation. The cover disc is parallel to the bottom disc. The flow and total pressure rise coefficients at the design flow conditions are ≈ 0.297 and

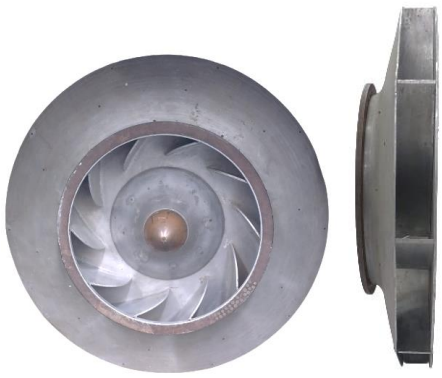

Fig. 2 Centrifugal fan rotor tested

Table. 1 Designs specifications for the tested rotor

Outlet diameter, D_5	*mm*	419.5
Inlet diameter, D_4	*mm*	207.6
Constant thickness, e_b	*mm*	3.0
Inlet angle, β_4	º	31.02
Outlet angle, β_5	º	50.41
Blade width, b_5	*mm*	32.1
Blades number, N	--	10
Volume flow rate	m^3/s	0.803
Pressure rise (in-out)	*Pa*	2739.162
Shaft power	*kW*	2322.647
Tangential velocity, u_5	*m/s*	65.894

≈1.147, respectively, with an efficiency of 94.7%, with the nominal rotating speed of n=3000$^{\pm 1}$ *rpm*, which are defined as:

$$\phi = \frac{Q}{AU_5} \tag{2}$$

$$\psi = \frac{2\Delta_{p_T}}{\rho U_5^2} \tag{3}$$

where Q, Δ_{p_T}, U_5, and ρ indicate the volume flow rate, total pressure rise, tangential velocity, air density, and A is the outlet area of the rotor.

The additional design conditions and specifications are listed in Table 1.

The experimental rig for measuring the fan aerodynamics is shown in Fig. 3. The rig consists of five main components: Test section, drive set, pressure equalization chamber, auxiliary unit, and measurement instrumentation. The rotor takes air from the environment and exhausts it into the equalization chamber (3). Afterward, the air is discharged from the chamber and passes through the orifice plate flow meter (5.1), suction pipe (4.1), auxiliary centrifugal fan (4.2), and flow control valve (4.3) before being released back into the environment. The experiments were conducted in accordance with the international standard ISO 5801 at Lab-Vent – UNIFEI.

The rotor to be tested is installed within the test section, as shown in Fig 3(b). This assembly consists essentially of 13 components as shown in Fig. 3(a):

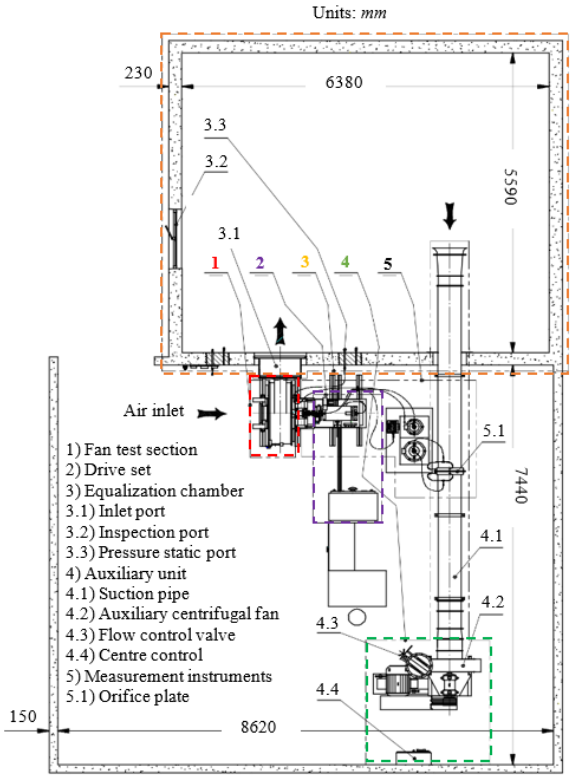

Fig. 3 Schematic diagram of test bench

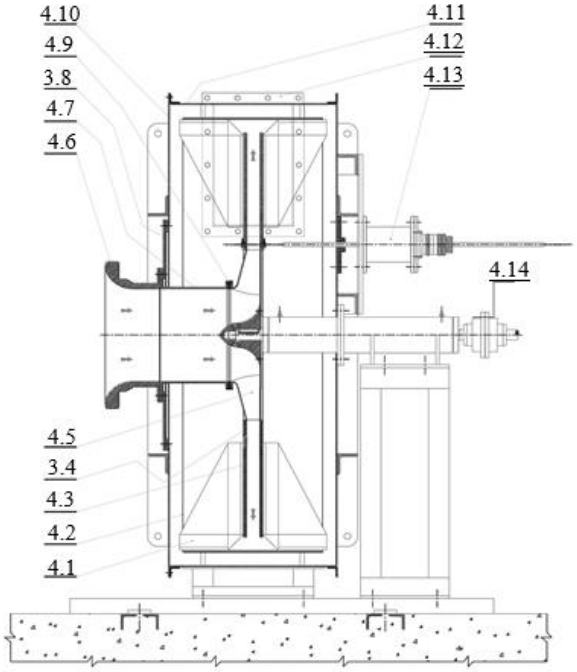

Fig. 3(a) Rotor test section scheme

diffuser support (4.1), circular ring (4.2), diffuser external disc (4.3), diffuser internal disc (4.4), centrifugal rotor (4.5), inlet nozzle (4.6), inlet duct (4.7), collector inlet mouth (4.8), rotor inlet labyrinth element (4.9), collector access door (4.10), collector (4.11), collector outlet (4.12) and the support for the probe movement mechanism (4.13). The bearing component (4.14) is mounted to support the centrifugal rotor being tested.

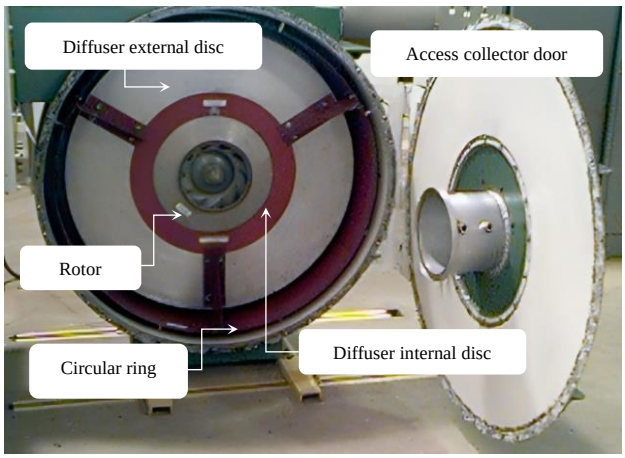

Fig. 3(b) Detail of the interior test section and the access door to the collector interior

The test section and the bearing component are fastened with screws and supported onto two "U"-shaped rails, allowing the positioning in relation to the drive assembly and the pressure equalization chamber, as highlighted in Fig. 3(b). The assembly composed of the inlet nozzle, inlet tube, collector inlet, and the labyrinth element of the rotor inlet is mounted on the access door to the collector interior using guide pins and a bolted connection. This entire assembly can be easily removed whenever access to the tested rotor is needed or when a replacement is required.

For rotors with external diameters D_5 larger than 500 *mm*, it is necessary to modify not only the dimensions of the inner disc of the diffuser but also the internal diameter of the outer disc. As a result, the diffuser diameter ratio, v_D, will be less than 2. To address this situation, the circular ring has been installed around the outer periphery of the diffuser. This ensures that the outlet port of the collector does not disrupt the rotor flow in an irregular manner. To ensure this interference is minimized, the diameter ratio of the diffuser, $v_D = D_{eD} / D_{iD}$, as seen in Fig. 4, should be at least 2, as recommended by Eckardt (1980).

2.2 Instrumentation and Measurement Procedures

Overall procedures involve measuring time-averaged values of various quantities related to the absolute flow at the rotor exit. To accomplish this, a single hole probe as employed by Westphal and Ortega (2004), was selected for its ability to accurately measure the velocity of the flow in a specific direction, especially considering that there is no need to measure velocity fluctuations. In the case of radial turbomachinery with specific rotation $n_{qA} < 200$, the axial component (c_a) of the absolute velocity in the rotor as shown in the Fig. 4 is relatively small when compared to the radial (c_r) and circumferential (c_u) components. In this situation the single-hole probe does not have the ability to measure c_a. In this case, the meridional component, c_m, responsible for the flow, will be approximated as only the radial component, c_r.

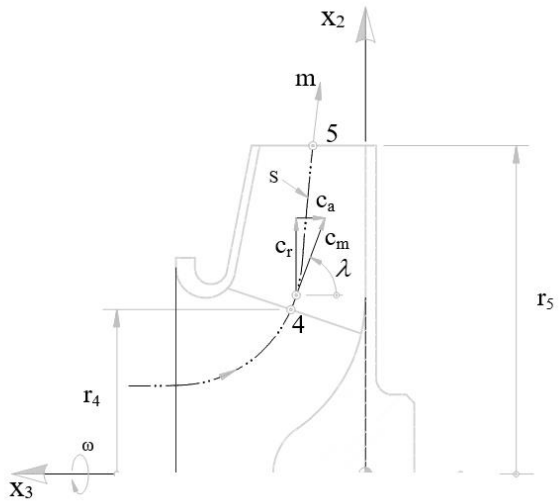

Fig. 4 Meridional section centrifugal rotor

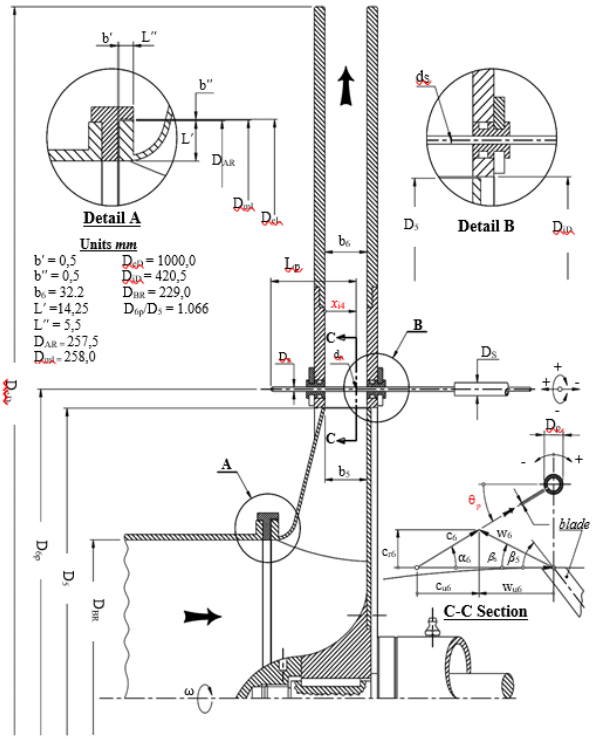

Fig. 5 Rotor meridian section showing probe placement within the diffuser

The probe is mounted in a bi-supported configuration through bearings located in the internal discs of the diffuser, with its centerline positioned at $D_{6p} = 447mm$ in relation to the rotor axis. The diffuser is comprised of two parallel discs separated with a uniform distance $b_6 = 32.2$ *mm* as shown in Fig. 5 and was placed concentrically on the rotor axis at its outer periphery. The purpose of this channel is to avoid irregular interference with the rotor flow from external components, such as the collector.

The probe is comprised of a circular section tube with an outer diameter of $D_p = 3mm$. It includes a radial hole with a diameter of $d_p = 0.35mm$, positioned at a distance

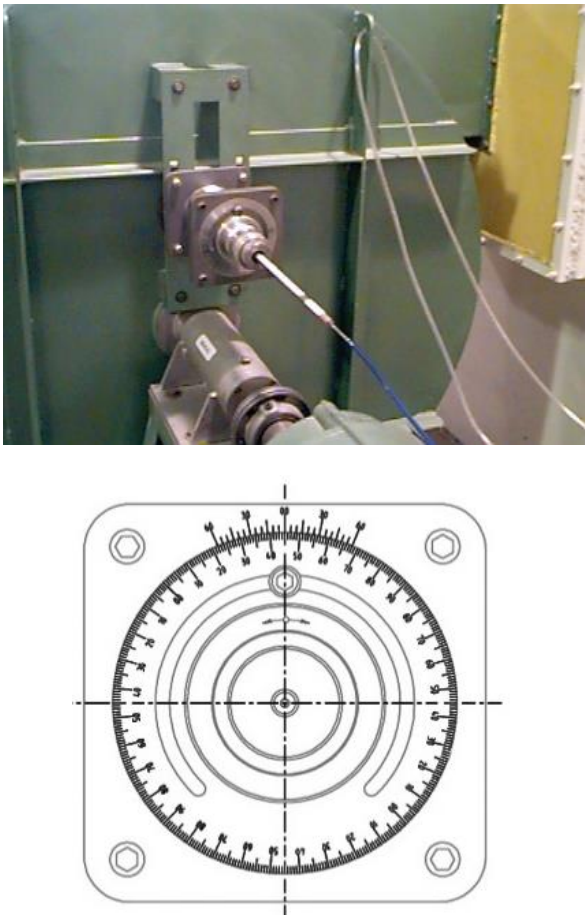

Fig. 6 Probe movement mechanism (upper), linear and angular vernier scale (bottom)

of $L_p = 65mm$ from one ends of the probe. At the opposite ends, there is the support tube, whose diameter is $D_S = 9.5mm$. This radial hole can be positioned as close as possible to the walls where the probe rests. It has the advantage of not suffering the tip effect as was observed by Ng and Ferguson (1983).

The probe has three different locations: one fixed (radial) and two with the ability to move (longitudinal and rotational). The movement mechanism helps to adjust it in the longitudinal position x_i . Rotational movements can be achieved with the assistance of an angular positioner, which features an angular vernier scale, allowing adjustments in 5° increments. This enables the probe to be positioned at different angular orientations θ_p in relation to the horizontal plane. This mechanism attached to the collector structure as shown in Fig. 6 allows an advancement of 1.5 *mm* per turn of the lead screw, and the fixation should be done with the linear vernier scale with 75 divisions (1 division ≡ 0.02 *mm*).

Were conducted several tests to evaluate the best number of points, m $(m = 2,3,...7)$ to covering a greater number of positions inside the diffuser channel. Considering the time spent conducting the tests and the accuracy of the results, we determinate $m = 4$ intervals that provided good precision to apply the Gauss-Legendre

Table 2 Probe longitudinal positions inside the diffuser channel

Positions	*mm*
x_{14}	2.236
x_{24}	10.626
x_{34}	21.574
x_{44}	29.964

numeric integration method, which uses a smaller number of intervals (or integration points, m) for our purposes.

Thus, for each fixed flow rate set, there are four longitudinal $x_{i4}(i = 1,2,3,4)$ and approximately 23 angular positions within the range of $^{\pm}135^{\circ}$ represented by θ_p for each longitudinal. While the probe was rotated around its axis at 5-degree intervals, each longitudinal position x_i was maintained to compose the flow pressure distribution points around the probe surface. These positions are identified by 1/4, 2/4, 3/4 and 4/4 and are shown in Table 2.

In the 1/4 position, the probe is near the external disc of the rotor and consequently at the point 4/4 is near the internal disc.

The flow pressure distribution curve derived from regression analysis in relation to the critical angle θ_c was obtained and plotted in Fig.7. Its exhibits a sinusoidal pattern that is proportional to the square of the sine of the polar angle, defined by Eq. 4:

$$h_{e6} = a_1 + a_2 \sin^2(a_3\theta_p + a_4) \tag{4}$$

where h_{e6} represents the pressure in mmH_2O provided by the probe for each θ_p , being:

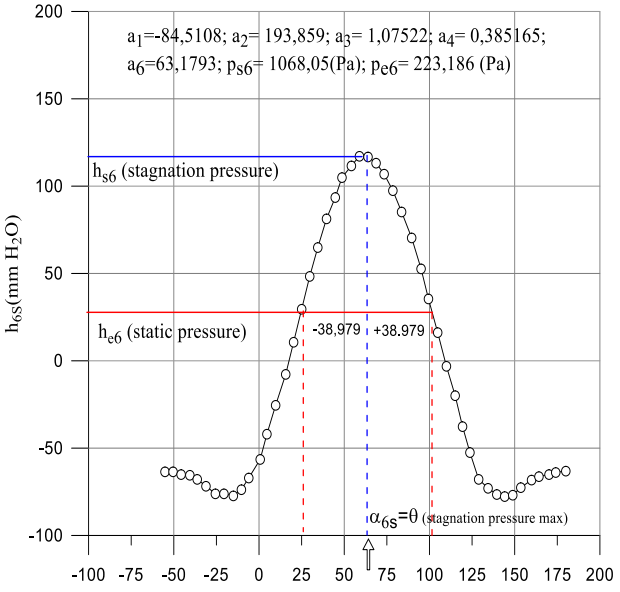

Fig. 7 Flow pressure distribution

$$\theta_p = \alpha_6 + \theta_c \tag{5}$$

being α_6 calculated by (6)

$$\alpha_6 = \theta_{p_{6i\,4\max}} = (\pi/2 - a_4)/a_3 \quad \text{in radians} \tag{6}$$

a_3 and a_4 are the constants of Eq. (4) for each probe position.

This model is based on the theory of potential flow around a cylinder with a constant cross-section of infinite length. This symmetric function centered accurately around the angle α_6 effectively fits the dataset through regression analysis to calculate the stagnation pressure, p_{s6} using the Eq.4. It is important for the pressure values to exhibit the highest degree of symmetry around this angle, this ensures minimal disparity between the measured values and those obtained through regression analysis. An almost linear behavior, but with steep slopes (high pressure gradients) can be noted in the region near this angle, this characteristic requires that the value of the critical angle be as accurate as possible to avoid distortions in the results.

According to Glaser (1952) and Benedict (1977), experiments conducted on spherical and cylindrical bodies indicate that the measured pressure is equal to the "true" pressure at a point located at a distance that depends on the diameter of the probe hole, d_p. (Benedict, 1977) recommends the value of $0,35d_p$, and thus, the correction angle k_p, in degrees, should be calculated by Eq. 7:

$$k = 0,35(360/\pi)(d_p/D_p) \tag{7}$$

The critical angle θ_c, was determinate by Eq. 8:

$$\theta_c = \theta_0 + k_p \tag{8}$$

where θ_c, which depends on the Reynolds number, is the angle between the stagnation pressure (maximum pressure provided by the probe) and the “true” static pressure. For the Reynolds number range $(4500 < R_e < 9000)$ in this work, and for the bi-supported mounted configuration probe, (Ng & Ferguson, 1983) indicate that the value of θ_0 is equal to 34.3°. Therefore, considering the dimensions of the probe, the value of k_s is 4.679°, which combined with θ_c results in the critical angle $\theta_c = 38.979^\circ$.

Three quantities are provided by the probe: The flow angle, α_6 the static pressure h_{e6} (p_{e6}), and the stagnation pressure h_{s6} (p_{s6}). These parameters were obtained for its each longitudinal position x_i as mentioned earlier. A total of 14 flow rate points were tested, reaching $4\times23\times14 = 1288$ pressure values.

The static pressure, p_{e6} is the most important parameter to determinate the absolute flow velocity vector c_6 and is obtained by shifting the angle α_6 from θ_c along the pressure distribution curve. Besides the probe a load

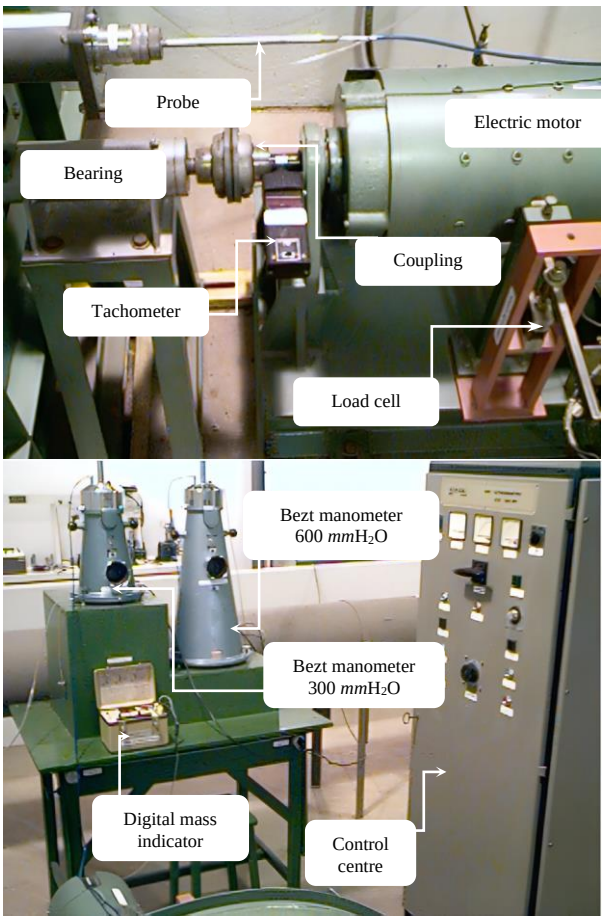

Fig. 8 Measurements instruments installation: pitot probe and load cell (upper), instrumentation (bottom)

cell as shown in Fig. 8 provides the mass values which are used in the calculation of aerodynamic characteristics of the rotor through shaft power of the DC electric motor.

The digital mass indicator displays the values of the mass m_{cc} acting in the load cell by the shaft power of the electric motor. This sensor was placed at a distance $L_b = 237mm$ equivalent to the arm of the electric motor casing, in line with the force action, as depicted in Figure 9.

To obtain the operating characteristics through shaft power P_e of the electric motor, one must subtract from this power, the power mechanical loss due to friction (mechanical and viscous) in the bearing and flexible

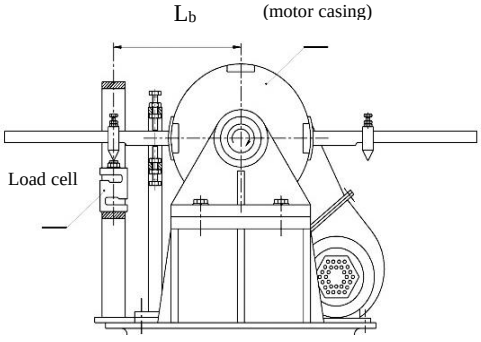

Fig. 9 Scheme of the DC electric motor and the action line of the load on the load cell

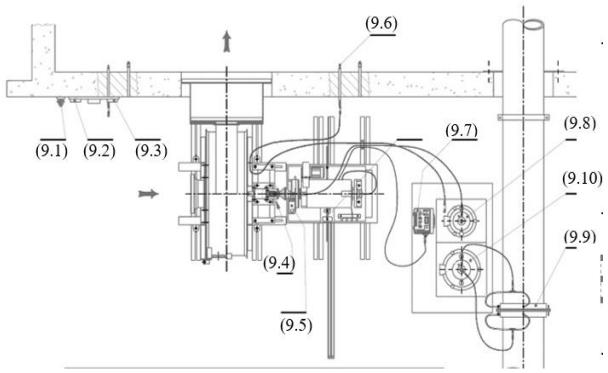

Fig. 10 Measurement instruments scheme

coupling, P_{mec}. This loss is determined by running the assembly formed by the electric motor, bearing, shaft, and flexible coupling without the centrifugal rotor for a rotation of $n = 3000^{\pm 1} rpm$. Thus, the power mechanical losses can be obtained by (9)

$$P_{mec} = 2\pi m_{mec} g L_b n \tag{9}$$

where $m_{mec} = 0.050kg$ is the mass acting when the electric motor rotates empty (without rotor), $g_{local} = 9.785 m/s^2$ is the local value of gravitational acceleration at the test bench location.

The values of flow quantities involved were simultaneously measured for the two adopted measurement systems. The measurements are performed by using all instruments shown in Fig. 10.

For each of longitudinal position of the probe, the values of the following quantities were read: 1) Longitudinal position of the probe in relation to the inner disc of the diffuser in *mm*, and position angle of the probe in relation to the horizontal plane θ_p in degrees, measured every 5° by using linear and angular vernier scale (9.4) respectively, 2) Local barometric pressure, through a Fortin barometer (9.1), (accuracy ±0.3 mmHg), 3) air temperature, measured through a digital thermometer (9.2), (accuracy ±0.1°C), 4) relative humidity, measured through a hygrometer (9.3), (accuracy ±0.5%), 5) Rotation of the centrifugal rotor using the digital optical tachometer (9.5), ($^{\pm}$1 rpm accuracy), 6) Mass acting on the load cell through digital mass indicator (9.7), 7) Pressure at the probe h_{6s} connected to the Betz manometer (9.8), (300mmH$_2$O) range, (accuracy ±0.1 mmH$_2$O), for each θ_p, values of h_{6s} are taken in a total of 20 to 26 values, 8) static pressure in the chamber, through chamber pressure port (9.6) and the static differential pressure Δ_h in the orifice plate flow meter at the outlet duct (9.9) were measured using the Betz manometer (9.10) of (600mmH$_2$O) range, (accuracy ±0.1 mmH$_2$O).

The air flow passing the test section is controlled with the help of the flow control valve. It was also determined using the Eq. 10, obtained by calibration, referring to the orifice plate flowmeter.

$$\dot{V}_{PO} = 0.066642\sqrt{\Delta_h / \rho_{air}} \tag{10}$$

In this expression, Δ_h is the difference in static pressures at the orifice plate, and ρ_{air} is the air density in *kg/m³*.

A study of uncertainties of all the variables involved in the experiment were considered following the guidance of (ISO 5168, 2005), the statistical uncertainties have a measurement dispersion limit set at a 95% confidence interval, and the results related to uncertainties are presented in percentage terms. All estimates uncertainties of direct measurements used in this work, as well as the values determination of different uncertainties, are described by de Oliveira (1999). These estimates were based on technical data from the various catalogs and manuals of the measurement instruments used and the recommendations by Figliola and Beasley (1991).

3. FAN PERFORMANCE

3.1 Aerodynamic Performance

The parameters values obtained from the experiments were computed using in-house codes written in MATLAB®, *TesteXY.m*, *Boxkan.m* and *Model.m*. The first code calculates the constants of Eq.4 with the input values of (θ_p, h_{6s}) and subsequently the values of α_6, h_{s6} and h_{e6} are calculated through the last two codes. Therefore, the following parameters are considered essential to describe the aerodynamic performance of the rotor.

Stagnation pressure

$$p_{s6} = \rho_{H_2O} g h_{s6} \tag{11}$$

- Static pressure at the rotor outlet

$$p_{s6} = \rho_{H_2O} g h_{e6} \tag{12}$$

- Absolute flow angle at the rotor outlet

$$\alpha_6 = \frac{180}{\pi}\left(\frac{\pi/2 - a_4}{a_3}\right) \tag{13}$$

- Absolute flow velocity at the rotor outlet

$$c_6 = [2(p_{s6} - p_{e6})/\rho_{air}]^{1/2} \tag{14}$$

- Radial component of the absolute velocity at the rotor outlet

$$c_{r6} = c_6 \sin\alpha_6 \tag{15}$$

- Absolute circumferential velocity component

$$c_{u6} = c_6 \cos\alpha_6 \tag{16}$$

- Total pressure coefficient

$$\psi = \frac{2Y}{\rho u_5^2} = \frac{2\Delta p_t}{\rho u_5^2} \tag{17}$$

where Y the specific work of the rotor, that is

$$Y = u_5 c_{u6} - u_4 c_{u3} \tag{18}$$

being $u_6 = \pi D_{6p} n_{i4}$ (19)

and $n_{i4} = \frac{1}{N_p} \sum_{J=1}^{j=N_p} n_j$ (20)

N_p represents the number of measured points for rotation, n, at each angular position of the probe. In this work c_{u3} was set to zero (no pre-rotation at the blade inlet).

- Flow coefficient

$$\phi = \frac{\frac{D_{6p} b_6}{D_5 b_5 f_{e5}} \tilde{c}_{m6}}{u_5} \quad \text{being} \quad f_{e5} = 1 - \frac{e_b N}{\pi D_5 sen\beta_5} \tag{21}$$

f_{e5} is the geometric choking factor at the blade outlet.

- Stagnation specific work

$$Y_s = \frac{\pi D_{6b} b_6}{2\dot{m}} \sum_{i=1}^{i=4} w_{i4} c_{m6} p_{s6} \tag{22}$$

where de values of weight coefficients w_i can be obtained from Zienkiewicz and Taylor (1989).

- Rotor efficiency

$$\eta_r = \frac{Y_s}{Y} \tag{23}$$

Some prediction methods have resulted in approaches that could provide slip factor predictions when combined with experimental studies like Guo and Kim (2003), Abdolahnejad et al. (2021) and Huang et al. (2013). Consequently, the experimental tests conducted aimed to determine the appropriate value of the slip factor (ε).

Considering a finite number of blades, the relative velocity flow angle is always smaller than the blade angle β_5 at the rotor outlet due to the Coriolis force. This angular deviation, which is responsible for the slip factor, results in velocity differences characterized by $\Delta c_u = |c_{u5} - c_{u6}|$. The slip factor definition from literature that is widely used to show this deviation is defined as follows:

$$\varepsilon = 1 - \frac{\Delta c_u}{c_{u5}} = \frac{c_{u6}}{c_{u5}} \tag{24}$$

If the absolute flow angle at the rotor inlet is 90°, the above mentioned definition can also be given via the relation between the rotor specific work Y / Y_∞, where Y is the real value for the energy transferred to the working fluid by the rotor blades, and the specific work, considering an ideal flow (an infinite number of blades), Y_∞ can be also calculated in terms of the pressure coefficient i.e.,

$$\varepsilon = \frac{Y}{Y_\infty} = \frac{\psi}{\psi_\infty} \tag{25}$$

where the rotor pressure coefficient ψ_∞, for blades of infinite thickness can be calculated according to:

$$\psi_\infty = 2 - k_\infty \phi \tag{26}$$

with the constant

$$k_\infty = \frac{2}{tg^{-1}\beta_5} \tag{27}$$

4. NUMERICAL APPROACH

The performance of the rotor is evaluated by the following three parameters: total pressure coefficient, ψ, slip factor ε, and the efficiency η.

A 3D steady numerical simulation of the flow through the rotor is performed. The numerical approach chosen to obtain the solution of the flow field was the Finite Volume Method implemented by the Ansys Fluent® 19.2. The flow was modeled by the Reynolds-Averaged Navier–Stokes equations coupled with the SST $k-\omega$ turbulence model.

Under these conditions, the conservation principles can be written in Cartesian coordinates and using index notation and assuming Einstein's sum convention as:

$$\frac{\partial u_i}{\partial u_i} = 0 \tag{28}$$

$$\rho u_j \frac{\partial u_i}{\partial x_j} = \frac{\partial}{\partial x_j}\left[-\rho \delta_{ij} + \mu \left(\frac{\partial u_i}{\partial x_j} + \frac{\partial u_j}{\partial x_i} \right) - \rho \overline{u_i' u_j'} \right] \tag{29}$$

Equation (27) and (28) are the continuity and the momentum equations, respectively.

The Reynolds' Stress $(-\rho \overline{u_i' u_j'})$ has been modeled considering the Boussinesq hypothesis, as a function of a turbulent viscosity (μ_t) and the turbulent kinetic energy (k):

$$-\rho \overline{u_i' u_j'} = \mu_t \left(\frac{\partial u_i}{\partial x_j} + \frac{\partial u_j}{\partial x_i} \right) - \frac{2}{3} k \delta_{ij} \tag{30}$$

The turbulence model applied to the problem is highly suitable for flows characterized by significant adverse pressure gradients and flow separation resulting from shear forces (Menter, 1992).

$$\mu_t = \frac{\rho k}{\omega \max\left[\frac{1}{\alpha^*}, \frac{sF_2}{\alpha_1 \omega} \right]} \tag{31}$$

$$\frac{\partial (\rho k)}{\partial_t} + \frac{\partial (\rho k u_i)}{\partial x_i} = \frac{\partial}{\partial x_j}\left(\Gamma_k \frac{\partial k}{\partial x_j} \right) + \tilde{G}_k - Y_k \tag{32}$$

$$\frac{\partial (\rho \omega)}{\partial_t} + \frac{\partial (\rho \omega u_i)}{\partial x_i} = \frac{\partial}{\partial x_j}\left(\Gamma_\omega \frac{\partial \omega}{\partial x_j} \right) + G_\omega - Y_\omega + D_\omega \tag{33}$$

In Equations (31) and (32), Γ represents the diffusivity of the turbulence variables, G and Y are terms associated respectively to the generation and dissipation of

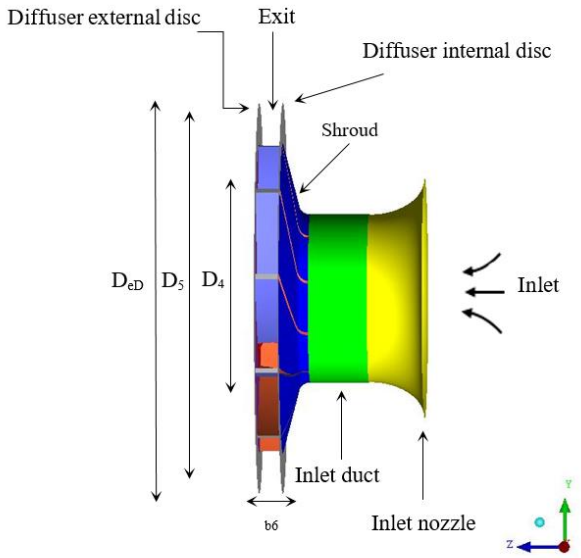

Fig. 11 3D Rotor computational domain

k and ω and D represents the cross-diffusion term. Fluent® Theory Guide (ANSYS 2013) contains further information about the modeling of these terms.

In the *SST* turbulence model by Menter (1992) is noted that the results of the $k-\varepsilon$ model are less accurate for large adverse pressure gradients. According to Versteeg and Malalasekera (2007), this model requires the use of spacing near solid walls on a fine grid to be able to accurately capture the profiles of the turbulent kinetic energy and its dissipation. In this context, (Menter, 1992) suggested a hybrid model using a transformation of the $k-\varepsilon$ model into a $k-\omega$ model.

The *SST* $k-\omega$ model changes the use of $k-\varepsilon$ model formulation in the presence of a high Reynolds in the regions most external to the domain walls using a mixing function that makes the activation in an appropriate way and selective use of these formulations without user intervention. This switching is achieved by blending the standard $k-\omega$ near solid walls with the standard $k-\varepsilon$ near the fully turbulent region far from the wall. The Reynolds stress computation and *k-equation* are the same as in Wilco's original $k-\omega$ model, but the ε - *equation* is converted into an ω equation by substituting $\varepsilon = k-\omega$. This approach is widely used in research fan works, such as Angulo et al. (2022), Heo et al. (2015) mong others.

4.1 Definition of Computational Domain

The computational domain Fig. 11 shows the three-dimensional model of the fan rotor implemented by the commercial software Ansys ICEM® 19.2. It is considered as a simplification of the experimental test section. It is divided into three domains: The non-rotating inlet (duct-nozzle), the rotating rotor, and the non-rotating outlet, composed by diffuser discs (internal-external). This configuration considers the radial channel placed concentrically on the rotor axis at its outer periphery to avoid irregular interference with the rotor flow from external components, in the same way as it was configured in the test section.

Regarding the numerical simulation, we started by calculating a steady flow using the frame motion approach. In this case, the relative position of the rotor and diffuser discs does not change during the calculations. For pressure and velocity coupling, the SIMPLE algorithm has been used with primary-order upwind scheme difference interpolation. The momentum equation, dissipation rate equation and turbulent kinetic energy equation were discretized with a second-order upwind scheme. The fluid is assumed to be steady, incompressible, with fluid density at the same value as in the experiments and a dynamic viscosity of $\mu = 1.7894\times10^{-5}$. The residual root means square (*RMS*) value of the governing equation was specified to be less than 10^{-4} to ensure the accuracy and convergence of numerical calculations.

4.2 Boundary Conditions

The center of the rotor is set as the origin of coordinates. To minimize the required computational effort for the simulation, we modelled only a single blade passage, and the symmetric condition is specified at the central plane and is applied based on the radial equilibrium hypothesis, according to Koupper et al. (2014), which is suitable for the determination of the flow field in a turbomachine and provides the balanced distribution of the flow properties from hub to casing between all blades.

The modeled boundary conditions were considered based on the results from experiment as follow:

Inlet surface: The velocity inlet was given on the inlet boundary based on the results from experiment, in magnitude normal to the surface such that the rotor operates at its design point. Also, an initial gauge pressure of 0 Pa and turbulence intensity level around 5% has been selected.

Outlet surface: The outlet condition was set as pressure equal to the atmospheric pressure. It is not necessary to establish any characteristic quantity of the flow such as

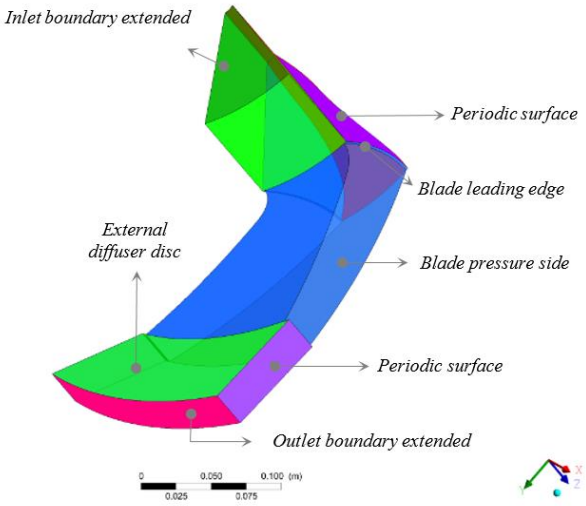

Fig. 12 Boundary conditions at rotor single blade passage

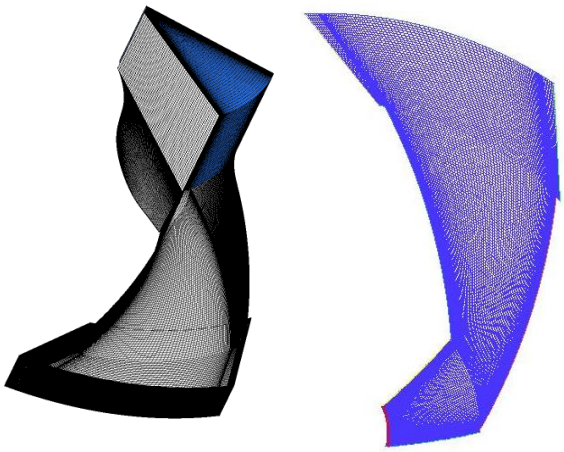

Fig. 13 Computational grid for a single blade passage; (left) and a plane at rotation direction refinement detail (right)

pressure or velocity at the outlet when this condition is used. The backflow turbulence intensity is 10% and the backflow turbulent viscosity ratio is ten.

Walls: The non-slip boundary condition, gravity effects are negligible and fluid properties are not functions of the temperature. This condition is used in the solid regions where the fluid circulates. The rotational movement of 314.16 *rad/s* in *Z*-direction of the total periodic domain is considered for the hub, casing, and blades. The stationary wall is chosen for the inlet and outlet domains.

The inlet and the outlet surfaces of the rotor have been extended to ensure numerical stability and to keep the incoming and outlet airflow uniform.

4.3 Mesh Generation

The meshing strategy consisted of a 3D high-quality hexahedral mesh, generated by the blocking structure technique by using Ansys ICEM® 19.2. A script in *Tcl/Tk* language was edited for the software interpretation, where the mesh growth functions was used to control the regions of high velocity gradients. The (left picture) in Fig. 13 shows the grid of whole blade channel computational domain, and grid refinement (right picture) is applied near the blade-to-blade pressure and suction sides, ensuring that the wall refinement is enough to provide an average wall distance $y^+ \approx 1$, recommended for the application of the *SST* $k-\omega$ turbulence model.

That is that the first node may be inside the viscous sublayer, which corresponds to a non-dimensional wall distance, defined by:

$$y^+ = \frac{u^* y}{\nu} \tag{34}$$

where u^* is the friction velocity, y is the distance of the first node to the wall and ν is the kinematic viscosity.

This way, the first elements are in the region of the viscous sublayer and, consequently, allowing to capture the velocity gradient close to the wall.

The distribution of y^+ values within the rotor domain, including the blades, ogive, and casing, was analyzed after

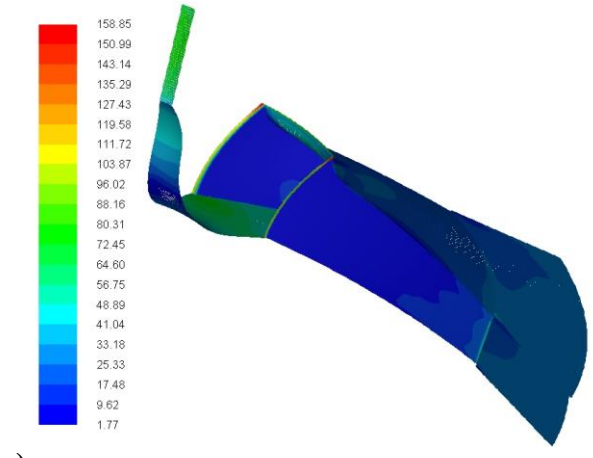

a)

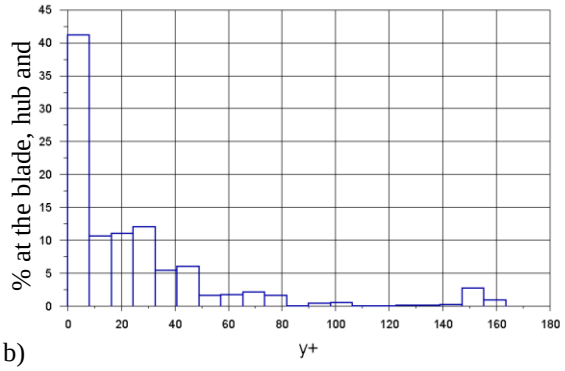

b)

Fig. 14 (a) y^+ Distribution contours and, (b) y^+ values bar graph for the rotor blade channel

Table 2 Mesh independence study

Mesh	Elements number	τ	η	ε_η	ε_τ
-	-	N-m	%	%	%
M	1 521 075	0.8809586	94.405	-	-
M_1	2 835 469	0.8758386	94.822	0.44	0.58
M_2	4 154 869	0.8805868	94.801	0.02	0.54

the calculation of the flow field, for the best efficiency point, where can see variations between 5 and 140, Fig 14(a). It indicates the presence of a refined mesh near the wall, where velocity gradients are in the laminar sub-layer, extending to the intermediate layer.

On the other hand, by analyzing Fig. 14(b), it is observed that larger regions of y^+ have values around 10.

The grid size plays a crucial role in influencing simulation outcomes. Therefore, it is imperative to assess grid independence to reduce the results sensitivity to mesh refinement. Three kinds of grid numbers were considered. The analysis results were achieved for the purpose of the study, as shown in Table 2.

The total efficiency and torque values were relatively well estimated with M_1, which is quite convenient from the point of view of the computational cost, especially considering the necessity of numerical simulations for comparing with measurements. A similar approach to assess mesh independence for turbomachinery was also explored by Angulo et al. (2022). The criterion for mesh independence was met when the percentage difference

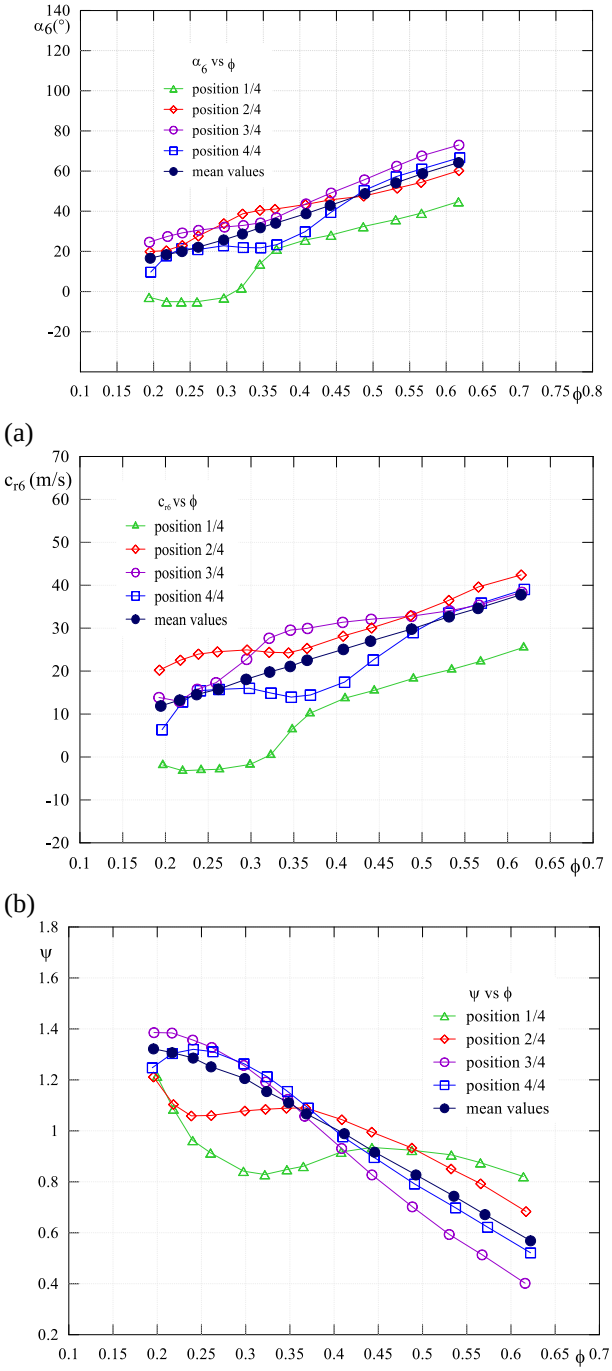

Fig. 15 (a) Absolute flow angle, (b) radial component of absolute velocity and (c) pressure coefficient through probe measurements Vs flow coefficient

between these global magnitudes for the refined M), coarse (M_1) and reference mesh (M_2) was less than 1%, thus, the mesh satisfies the criterion of independence. Finally, this study utilized a mesh comprising 2.8 million cells for the simulations.

5. RESULTS AND DISCUSSIONS

In this section, the aerodynamic characteristics of the rotor obtained through our experimental measurements are presented, along with a numerical results comparison.

As mentioned earlier two measurement systems were employed to gather data on the aerodynamic characteristics of the rotor studied. The results are presented for a wide range of the flow coefficient and are divided in two parts: the first one is related to the local and mean flow quantities obtained with the aid of the probe, while the second is related to the global quantities obtained through the load cell.

5.1 Probe Measurement Results

Local values for the absolute flow angle (α_6), radial component of absolute velocity (c_{r6}), pressure coefficient (ψ) and slip factor behavior, (ε) are shown in Fig. 15(a)-(c). Additionally, the average values for each quantity are shown on the same graph.

The minimum values of ϕ were obtained near those corresponding to the volumetric surge limit, while the maximum values were reached with the auxiliary centrifugal fan running and the flow control valve fully open. Therefore, for higher values of ϕ, extremely low static pressures at the rotor outlet could be obtained, even reaching negative values.

As shown in Fig. 15(a), the local values of α_6 are negatives for the 1/4 position of the probe, within a small range of flow coefficient. This situation indicates that there was flow reversal at the rotor outlet on the side corresponding to its external disc. If we assume an increase of the number of blades, the range of negative values of ϕ would also increase. This characteristic would be expected because when the number of blades is increased, the pressure developed by the rotor would increase mainly at the outlet, making the fluid flow through the rotor more challenging.

Figure 15(b) shows the values of the local and mean radial components of the absolute velocity c_{r6} at the rotor outlet. As expected, the same behavior described above for the 1/4 position, concerning the flow reversal at the outlet, should be observed for c_{r6}. It is also noted that, for the other corresponding probe positions, there is a similar trend between the values of c_{r6} and α_6.

Figure 15(c) shows measurements taken at the same positions of the probe. The c_{u6} values are correlated with values of ψ, and exhibit similar behaviors across all probe positions.

For demonstration purpose, an alternative way to show the values of α_6, c_{u6} and c_{r6} can observe in Fig. 16. These profiles at the rotor outlet are showed as a function of the diffuser width. In the plot, each longitudinal probe position x_i is represented by a green point that shows the location where the probe is rotated around its axis to compose the flow pressure distribution curve mentioned earlier.

One can notice that Fig. 16 is comprised of horizontal lines. This is just a more representative manner of showing

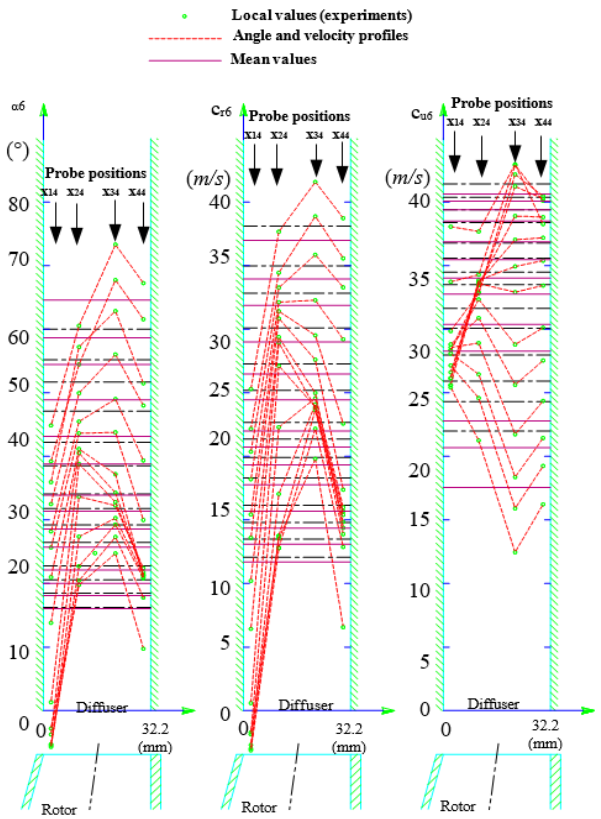

Fig. 16 Velocities profiles and outlet flow angle as a function of diffuser width

the mean values of the quantities α_6, c_{u6}, and c_{r6} plotted in the previous figures.

The local and mean values of the slip factor are represented in Fig. 17. It can be observed that for higher values of ϕ, starting from a certain point, the ε values for each longitudinal probe position spread increasingly, indicating a significant variation across the blade width. Furthermore, at higher ϕ, ε decrease for the 2/4, 3/4, and 4/4 positions. This decreasing trend in ε, even for only 2/4, 3/4, and 4/4 positions, results in a more pronounced reduction in the mean slip factor value for highest ϕ, due to the weighting coefficients in the Gauss-Legendre numerical integration are higher for the 2/4 and 3/4 positions.

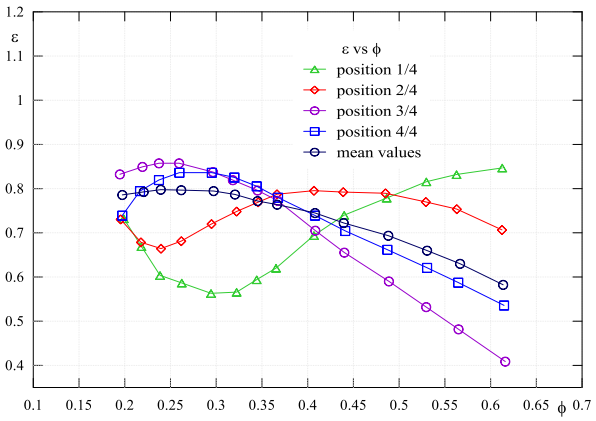

Fig. 17 Local and mean slip factor through probe measurements Vs flow coefficient

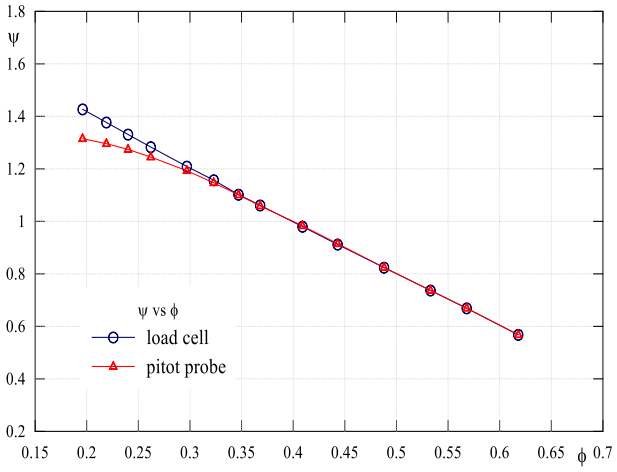

Fig. 18 Comparison of pressure coefficient Vs flow coefficient between two measurement systems

5.1 Measurement Results from the Load Cell

In this section, we will analyze in more detail the measurements result from the load cell and a comparison with the measurements through the probe.

Figure 18 shows pressure coefficients obtained through the load cell compared with the probe ones. For values of $\phi < 0.323$ the characteristic of the pressure coefficient in the analyzed range is always ascending, unlike the results through the probe.

This trend is due to the so-called flow recirculation inside the rotor. In this region, the rotor specific work (or, alternatively, the pressure coefficient) calculated from the shaft power (via load cell) is greater than that calculated from the flow measurement (via probe). The difference represents the energy losses due to this phenomenon.

The slip factor and rotor efficiency depend on ψ. Therefore, it is expected that, for values of ψ (probe) and ψ (load cell), as well as for η (probe) and η (load cell), similar behaviors will occur. In other words, values will be nearly coincident for $\phi > \phi_{opt} = 0.323$, and they will diverge for small values of ϕ. These behaviors are shown in Fig. 19 and 20.

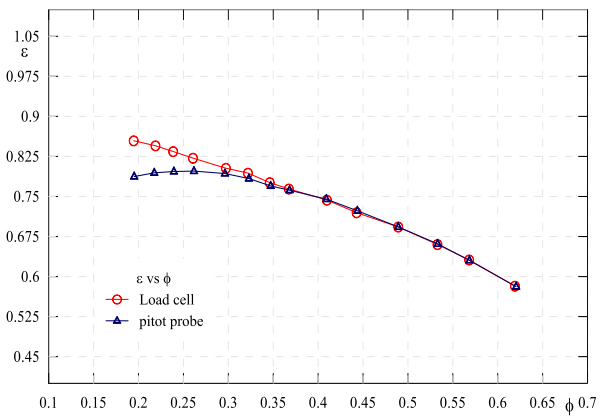

Fig. 19 Comparison of slip Factor Vs flow coefficient between two measurement systems

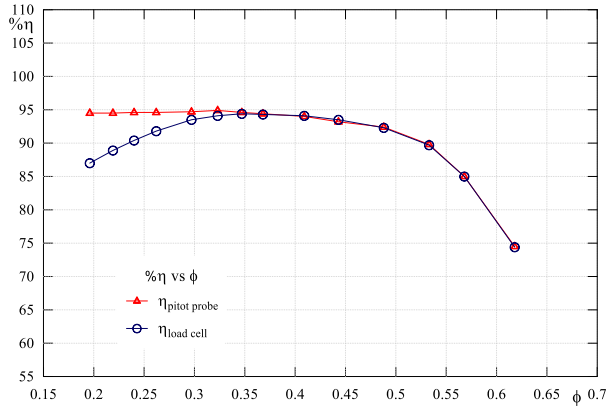

Fig. 20 Comparison of total efficiency Vs flow coefficient between two measurement systems

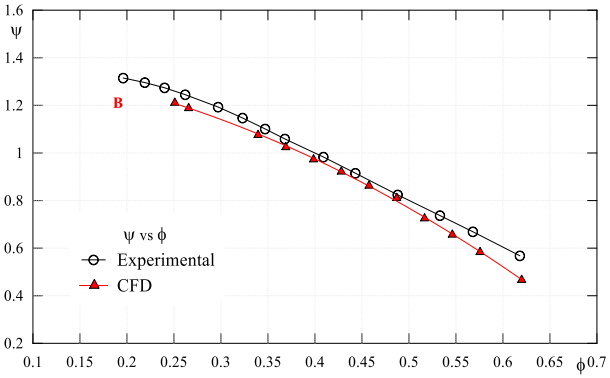

Fig. 23 Comparison of numerical and experimental pressure coefficient Vs flow coefficient

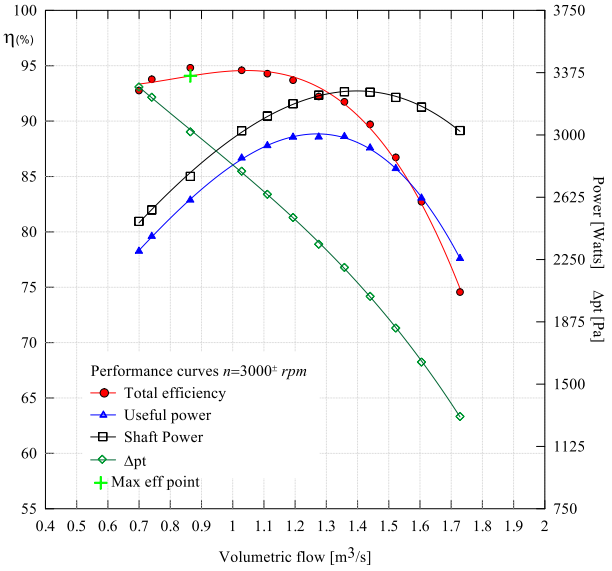

Fig. 21 Characteristic curves of the performance of the centrifugal rotor operating at 3000 *rpm*

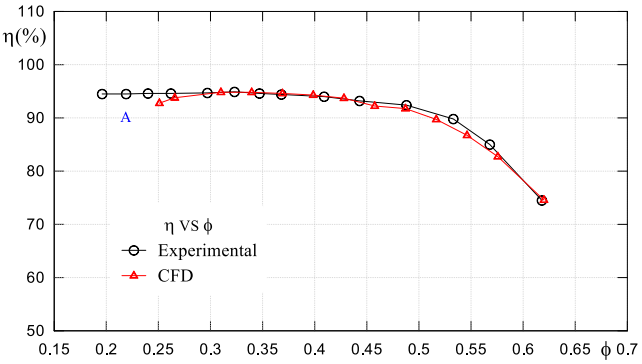

Fig. 22 Efficiency comparison between experimental and numerical results for the rotor operating at 3000*rpm*

5.2 Global Quantities

Numerical simulations are conducted for detailed flow visualization and dimensionless quantities such as ε, ψ, and η were also analyzed with flow coefficient.

The characteristic curves of the centrifugal rotor obtained through simulations are shown in Fig. 21. Once defined the surfaces on which the total pressures are weighted by mass average, the useful power is obtained thought the flow field analysis tool (*turbo-topology*) by commercial software Fluent®, resulting the rotor efficiency as the relationship between the useful power $P_h = \dot{V}\Delta_{Pt}$ and the shaft power $P_e = \Omega M$

The shaft power is reported based on the moment through the integration of pressure and shear stress on the specified surfaces that defines the rotor domain (hub, shroud, and blade) with respect to a non-inertial reference system and the moment in the direction of the rotation axis.

From the figure one can see that the volumetric flow of $\dot{V} = 0.86 m^3/s$, $\approx \phi = 0.309$ yielded a total efficiency around $\eta = 94.82\%$, a shaft power of $P_e = 2751.52[W]$ and an useful power of $P_h = 2609.06[W]$ which correspond to the total pressure rise of $\Delta_{Pt} = 3019.366$ [Pa]. Rotor efficiency is one the most important and direct global quantity that characterize the centrifugal rotor performance. Based on experimental results the rotor efficiency can be obtained. Then, the Fig. 22 shows the rotor efficiency curve that had in good agreement with measurements values in a large range of flow rates. Nevertheless, it is essential to highlight the region (A) of flow instability for flow rates values under $\phi \cong 0.25$ that arises from pressure fluctuations on the blade surfaces, resulting flow recirculation that affects the modeled convergence criteria for simulations.

Figure 23 shows comparisons for total pressure coefficient with experimental ones. It can be observed that approximately to $\psi = 1,079$, around $\phi \cong 0.309$ at the best efficiency point (B.E.P) the two curves are very close each to other and closely aligns with the experimental measurements, demonstrating a relative deviation within 0.113% of the measured data except at the same region (B) due to the convergence instability of simulations for flow rates under $\phi \cong 0.25$.

After verifying the deviation between the blade angle and the relative flow angle at the rotor outlet in both measurements and simulations, the slip factor behavior curves are compared and presented in Fig. 24.

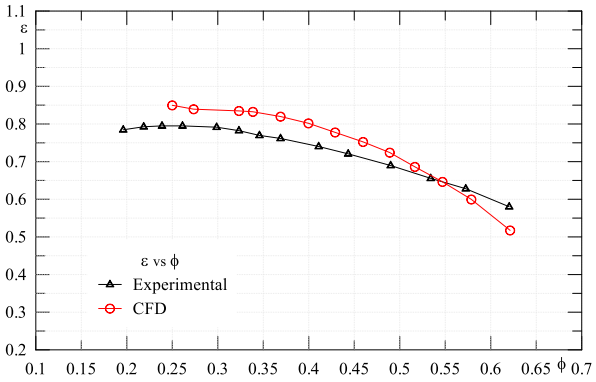

Fig. 24 Comparison of Numerical slip factor and probe measurements Vs flow coefficient

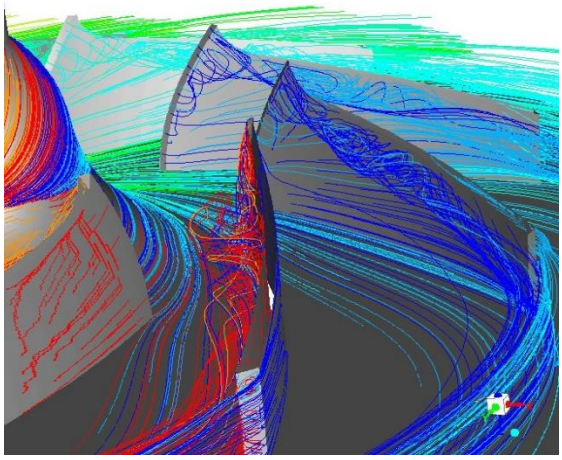

Fig. 25 Airflow visualized with instantaneous streamlines

From the figure can be observed that both curves exhibit slightly variations in trend in the high flow coefficient range. These divergences also appear in the range of low values of ϕ, established by the presence of the volumetric surge limit. In qualitative terms, both curves exhibit the same trend in the range between the flow coefficients $\phi \cong 0.309$ and $\phi \cong 0.42$, highlighting the suitability of the experimental method to predict the slip factor based on corresponding geometric parameters such as blade shape and flow coefficient.

It is important to note that this dependence also highlights the inadequacy of the empiric and semi-empiric formulas used in conventional practice to predict the slip factor, such as the expressions by Pfleiderer (1960), Eck (1973), Stodola et al. (1927), Stanitz (1952) and Wiesner (1967). In the particular case the expression by Wiesner (1967) which is still cited as the one that best predicts the slip factor in centrifugal impellers is only suitable for the case of logarithmic blades with a constant width along the radius, this inconsistency will undermine the accurate computation of the real value of the rotor specific work.

5.3 Local Flow Field Analysis of the rotor

In this section, visualizations of the rotor flow field are presented with particular emphasis on results discussed in section 5.1. The comparisons of ψ, η and ε, between the two measurements systems showed variations at small values of flow rates. The main reason is that the flow recirculation within the rotor is not sensed by the probe located downstream of the rotor.

This phenomenon can be visualized with the behavior of the velocity streamlines in the blade passage shown in Fig. 25 that is associated as strong evidence for separated flow which happens at the blade leading edge. The separation vortex continues to develop along the blade path, due to the boundary layer separation, which will cause the deterioration of the downstream flow field. Consequently, a minor recirculation is evident at the blades trailing edge.

5. CONCLUSIONS

This study experimentally and numerically performed quantitative analysis and examination of various flow characteristic of a voluteless centrifugal fan rotor. The studied variables included slip factor, absolute flow angle, pressure coefficient, total efficiency, and radial component of absolute velocity at the rotor outlet.

We reached the following conclusions through analysis and discussion:

- Despite the single hole probe does not immediately provide values for stagnation and static pressures, as well as the flow angle, as is the case with two or three-hole probes, on the other hand, many points facilitate obtaining the curve equation determined through the nonlinear parameter estimation technique. With this technique, it was possible to adopt a sinusoidal equation as a model for parameter estimation. Due to the symmetrical nature of this equation, it was possible to accurately determine the stagnation pressure, flow angle, and a single static pressure value for each longitudinal position of the probe, avoiding undesirable points outside the curve.
- The results by the probe and the load cell showed very good agreement for flow rates larger than those at the design point, reflecting the remarkable quality of the tests. Load cell measurements provided results revealing the flow recirculation phenomenon within the rotor, which is not detected by the probe located at the exit.
- For subsequent studies, we recommend the implementation of multiple-hole probes that would be placed near the entrance and exit of the rotor to measure the absolute flow. One probe would be positioned in place of the single hole probe, and the other would be placed near the entrance of the rotor. For this purpose, not only was the location for positioning the probe at the entrance built in this study, but also its movement mechanism. In principle, tests could be conducted on the same rotor analyzed in this work. In addition to the more accurate flow rate mentioned earlier, the specific work of the rotor, $Y = u_5 c_{u6} - u_4 c_{u3}$, could be more accurately obtained for the entire flow range. A comparison between the

results obtained in this study and those with multiple-hole probes would be useful to show the implications arising from not considering the axial, c_a, and circumferential, c_{u3}, components.

- With a multiple-hole probe located at the inlet and another at the outlet, the recirculation of the flow could be measured both at the inlet and the outlet of the rotor for low flow rates. Once again, measurements through the load cell would be useful for the purpose of comparisons. With the probe located at the inlet, the pre-circulation of the flow could be measured across the entire flow range. Anticipating such a scenario, the special test section was designed in a way that an appropriately sized tube (for better flow uniformity at the entrance of the rotor) can be inserted between the components (4.6) inlet nozzle and inlet tube (4.7), Fig. 3a.
- Several centrifugal rotors could be built with the same meridional shape and the same constructive angles of inlet and outlet of the blade. In principle, blades with constant thickness could be constructed, based on the midline of the blades of the rotors shown in Fig. 1.
- CFD results are quite close to experimental ones. It can be noted that the SST $k-\omega$ turbulence model has the merits to represent appropriate dissipative effects of turbulent viscosity for internal flows in turbomachinery channels.

ACKNOWLEDGEMENTS

The authors would like to thank the members of the Mechanical Engineering Institute at the Federal University of Itajubá (IME-UNIFEI), the Virtual Hydrodynamic Laboratory (LHV), and the Coordination for the Improvement of Higher Education Personnel (CAPES), for their financial support.

CONFLICT OF INTEREST

The author(s) declared no potential conflicts of interest with respect to the research, authorship, and/or publication of this article.

AUTHORS CONTRIBUTION

D.O. Maestre Di Cioccio: Conceptualization, Methodology, Software, Validation, Writing - original draft, Writing - review & editing. **R.G. Ramirez Camacho**: Methodology, Software, Resources, Supervision, Writing - review & editing. **W. de Oliveira**: Conceptualization, Experimental tests execution, Supervision, Writing - review & edit.

REFERENCES

Abdolahnejad, E., Moghimi, M., & Derakhshan, S. (2021). Experimental and numerical investigation of slip factor reduction in centrifugal slurry pump. *Journal of the Brazilian Society of Mechanical Sciences and Engineering*, *43*(4), 1–14. https://doi.org/10.1007/s40430-021-02831-x

Angulo, T. M. A., Camacho, R. G. R., de Oliveira, W., da Silva, E. R., & Río, G. E. N. (2022). Free and Non-Free vortex design for axial fans with circumferential sweep through CFD techniques. *Journal of Applied Fluid Mechanics*, *15*(4), 1017–1034. https://doi.org/10.47176/jafm.15.04.33209

Ansys Inc. (2012). Ansys Fluent Theory guide. USA.

Benedict, R. P. (1977). *Fundamentals of temperature, pressure, and flow measurements*. John Wiley & Sons, Inc. https://doi.org/10.1017/S0022112078211780

Carolus, T. H., McLaughlin, D. K., & Basile, R. (2000, July). *Experimental investigation of the unsteady discharge flow field and the noise of a centrifugal fan impeller*. 7th International Congress on Sound and Vibration. https://doi.org/10.3390/pr11072116

Cui, H., & Chen, C. (2017). *Effects of the installation of driven motor at the impeller eye on performance of volute-free centrifugal fan.* ASME International Mechanical Engineering Congress and Exposition, Vol. 50619, V007T09A081. https://doi.org/10.1115/IMECE2016-67609

Datong, Q., Yijun, M., Xiaoliang, L., & Minjian, Y. (2009). Experimental study on the noise reduction of an industrial forward-curved blades centrifugal fan. *Applied Acoustics*, *70*(8), 1041–1050. https://doi.org/10.1016/j.apacoust.2009.03.002

de Oliveira, W. (1999). *Características do escoamento em rotores centrífugos, Parte I: Análise teórica, Parte II: Análise experimental", DME/IEM/EFEI, Itajubá, MG*.

Eck., D. I. B. (1973). *Design and operation of centrifugal, axial-flow and cross-flow fans.* Pergamon Press

Eckardt, D. (1980). *Flow field analysis of radial and backswept centrifugal compressor impellers. Part 2: comparison of potential flow calculated and measurements.* Twenty-Fifth Annual International Gas Turbine Conference. https://ui.adsabs.harvard.edu/abs/1979ppcp.proc...77E/abstract

Figliola, R. S., & Beasley, D. E. (1991). Theory and design for mechanical measurement. https://doi10.1088/0957-0233/12/10/701

Glaser, A. H. (1952). The Pitot cylinder as a static pressure probe in turbulent flow. *Journal Sciences Instruments*, *29*, 219–221. https://doi10.1088/0950-7671/29/7/306

Guo, E. M., & Kim, K. Y. (2003). *Three-dimensional flow analysis and improvement of slip factor model for forward-curved blades centrifugal fan*. Proceedings of the ASME/JSME Joint Fluids Engineering Conference, 2 B, 1203–1211. https://doi.org/10.1115/fedsm2003-45404

Heo, M. W., Kim, J. H., & Kim, K. Y. (2015). Design optimization of a centrifugal fan with splitter blades.

International Journal of Turbo and Jet Engines, *32*(2), 143–154. https://doi.org/10.1515/tjj-2014-0026

Huang, J. M., Luo, K. W., Chen, C. F., Chiang, C. P., Wu, T. Y., & Chen, C. H. (2013). Numerical investigations of slip phenomena in centrifugal compressor impellers. *International Journal of Turbo and Jet Engines*, *30*(1), 123–132. https://doi.org/10.1515/tjj-2012-0021

ISO 5168 (2005). *Measurement of fluid flow - Evaluation of uncertainties. British Standards Institution.* https://www.iso.org/standard/32199.html

ISO 5801 (2017). *Performance testing using standardized airways.* https://www.iso.org/standard/56517.html

Koupper, C., Poinsot, T., Gicquel, L., & Duchaine, F. (2014). Compatibility of characteristic boundary conditions with radial equilibrium in turbomachinery simulations. *AIAA Journal*, *52*(12), 2829–2839. https://doi.org/10.2514/1.J052915

Meakhail, T., & Park, S. O. (2004). *A study of impeller-diffuser-volute interaction in a centrifugal fan.* Turbo Expo: Power for Land, Sea, and Air. https://doi.org/10.1115/GT2004-53068

Menter, F. R. (1992). Influence of freestream values on k-ω turbulence model predictions. *AIAA Journal*, *30*(6), 1657–1659. https://doi.org/10.2514/3.11115

Ng, C. K., & Ferguson, T. B. (1983). *A note on the blockage of cylindrical probes.* Proceedings of the Seventh Conference on Fluid Machinery.

Ottersten, M., Yao, H. D., & Davidson, L. (2021). Tonal noise of voluteless centrifugal fan generated by turbulence stemming from upstream inlet gap. *Physics of Fluids*, *33*(7), 1–16. https://doi.org/10.1063/5.0055242

Ottersten, M., Yao, H., & Davidson, L. (2018). *Unsteady simulation of tonal noise from isolated centrifugal fan.* Proceedings of Fan 2018 - International Conference on Fan Noise, Aerodynamics, Applications and Systems. https://doi.org/10.31224/osf.io/yx7rj

Pfleiderer, C. (1960). *Bombas centrífugas y turbocompresores* (Editorial Labor S. A.).

Stanitz, J. D. (1952). Some theoretical aerodynamics investigations of impellers in radial and mixed flow centrifugal compressors. *Transactions of the ASME*,. *74*, 473–497. https://doi.org/10.1115/1.4015817

Stodola, A. Bohuslav, & Loewenstein, L. Centennial. (1927). *Steam and gas turbines : with a supplement on The prospects of the thermal prime mover*. New York: McGraw-Hill.

Versteeg, H. K., & Malalasekera, W. (2007). *An introduction to computational fluid dynamics: the finite volume method.* Pearson education.

Wei, Y., Zhu, L., Zhang, W., & Wang, Z. (2019). *Numerical and experimental investigations on the flow and noise characteristics in a centrifugal fan with step tongue volutes*. https://doi.org/10.1177/0954406219890920

Westphal, R. V., & Ortega, A. (2004, July). *Cascade throat flow measurements using a rotatable single-hole pressure probe.* 24th AIAA Aerodynamic Measurement Technology and Ground Testing Conference. https://doi.org/10.2514/6.2004-2601

Wiesner, F. J. (1967). A review of slip factors for centrifugal impellers. *Journal of Engineering for Gas Turbines and Power*, *89*(4), 558–566. https://doi.org/10.1115/1.3616734

Zeleke, W. A., Hughes, T. L., & Drozda, N. (2020). Home–school collaboration to promote mind– body health. In C. Maykel & M. A. Bray (Eds.), *Promoting mind–body health in schools: Interventions for mental health professionals* (pp. 11–26). American Psychological Association. https://doi.org/10.1037/0000157-002

Zhang, J., Chu, W., Zhang, H., Wu, Y., & Dong, X. (2016). Numerical and experimental investigations of the unsteady aerodynamics and aero-acoustics characteristics of a backward curved blade centrifugal fan. *Applied Acoustics*, *110*, 256–267. https://doi.org/10.1016/j.apacoust.2016.03.012

Zienkiewicz, O. C., & Taylor, R. L. . (1989). *The finite element method*. ISBN: 0 7506 5055 9.